ACTA METALLURGICA SLOVACA
2022, VOL. 28, NO. 4, 212-218

RESEARCH PAPER

EFFECT OF RETAINED AUSTENITE ON PLASTIC CHARACTERISTICS OF DUAL PHASE STEELS

*Peter Prislupčák[1,2)] *, Tibor Kvačkaj[3)], Jana Bidulská[2)], Stanislav Németh[1)], Mária Demčáková[1)], Roman Gburík[1)] Vladimír Kundracík[1)]*

[1)] U. S. Steel Košice, s.r.o., Research and Development USSE, Košice, Slovakia
[2)] Technical University of Košice, Faculty of Materials, Metallurgy and Recycling, Košice, Slovakia
[3)] Bodva Industry and Innovation Cluster, Moldava nad Bodvou, Slovakia

[*]*Corresponding author: peterprislupcak@sk.uss.com; +421 917097744; U. S. Steel Košice, s.r.o., Research and Development USSE, Vstupný areál U. S. Steel, 044 54 Košice, Slovakia*

Received: 18.11.2022
Accepted: 05.12.2022

ABSTRACT

In terms of the current trend of research and development of new materials and optimization of current materials in the automotive industry, the greatest attention is paid to progressive high-strength dual-phase (DP) steels with increased stampability, which are designed for cold stamping for specific internal car body components of the current market. New grades of DP steels provide a combination of high strength and good formability and contribute to the weight savings of vehicle parts by 10 to 20 %, compared to current DP grades. Thanks to their top properties, DP steels with increased formability can absorb more crash energy using less steel. As a result, high-strength DP780GI and DP780GI-HF materials of first generation (hereinfater DP780GI-HF) were analyzed. The stampability improvement of DP steels was demonstrated by the experimentally determined Forming Limit Curves for both steels.

Keywords: Forming Limit Curve, residual austenite, microstructure, numerical simulations

INTRODUCTION

In recent years weight savings design and passengers' safety are the main goals in the automotive industry. Advanced high strength steels (AHSS) especially dual phase steels (DP) combine a favorable ratio between high formability and strength. Their mechanical properties offer a great potential for further development of automobile bodies [1-4]. According to their tensile strength levels DP steels show a low yield strength and high work hardening. Microstructure of DP steels containing hard martensite islands (up to about 25 volume %) dispersed in a soft and ductile ferrite matrix [5-7]. In DP steels besides the martensite retained austenite might be detected [2, 8]. The mechanical properties of the DP steels are largely affected by the amount, morphology, size, carbon content, and distribution of the martensite phase and also ferrite grain size [9-14].

The possibilities for production of DP steels can be divided to two groups: Top_Down resulting from hot processes follows by austempering and Bottom_Up resulting from cold deformations follows by intercritical annealing and cooling [2, 4, 12].

Based on performed research [5] where DP steels were experimentally oil-quenched from various temperatures it was found that the content of retained austenite increased with temperature in the intercritical range. This phenomenon was understood on the basis of growing amount of austenite with the temperature and carbon content. An additional effect was a decrease in the size of the austenite grains which effectively stabilizes the austenite in contradiction of martensite transformation. It was also found that the retained austenite was enormously stable on further cooling to lower temperatures, while during plastic deformation it quite readily transformed to martensite [5]. Several studies have methodically studied the effect of volume fraction of martensite on mechanical properties of DP steels. It was exposed that the strength rises, and total elongation declines by growing the amount of martensite in steels with carbon contents between 0.05 and 0.4 wt%. The main focus was to achieve DP steels with high strength and acceptable formability with low carbon content. In view of the low hardenability associated with low carbon content, the relatively high manganese content of the steel provides sufficient hardenability to produce fully martensitic microstructure after quenching from the austenitic regions [4, 7, 14, 15]. Although DP steels have promising mechanical properties, there is a request to optimize their properties to improved combination of strength and ductility [11, 12]. Formability of the steels is one of the most crucial factors in the forming process. The forming limit is an important processing parameter in the sheet metal forming field, reflecting the maximum deformation degree before cracking in the formed material [2, 13-16]. A way to determine if the certain steel grade has sufficient formability to make a part is to use a forming limit diagram [17-19]. Forming limit diagrams (FLDs) are one of the most helpful and used tool for assessing the workability of metal sheets. FLDs provide the failure locus at the onset of necking (commonly designated as the forming limit curve [FLC]) and at the onset of fracture in the principal strain space [17, 20, 21]. As shown in **Fig. 1**, a FLD is separated into

different zones by several curves. The vertical and horizontal axes correspond to the major and minor strains, respectively. At any instant during a forming process, the strain at each position on the sheet is characterized as a point in the forming limit diagram. The formability of the sheet can be assessed by comparing the locations of these points to the curves [19, 21].
The strain hardening exponent (n-value) varies for most steels from 0 to 0.3, with higher values being indicative of higher formability and improved ability to distribute strains and avoid necking [2, 17, 18]. This work is focused on finding relation of retained austenite on plastic characteristic of dual phase steels with the minimal tensile strength 780MPa.

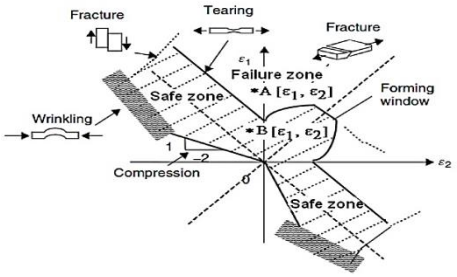

Fig. 1 Scheme of Forming Limit Diagram [21]

EXPERIMENTAL MATERIALS AND METHODS

Experimental research was carried out on standard samples of sheets with the thickness of 1.2 mm of grades DP780GI and DP780GI-HF of the first generation (hereinafter referred to as DP780GI-HF). The chemical composition (**Table 1**) of both grades, which meet the limits required by VDA 239:100 (05/2016), was determined on OBLF QSG 750 analyzer (OBLF, Witten, DE, Germany) by Optical Emission Spectral Analysis. The main difference between the DP780-GI and DP780GI-HF steel grade is in the chemical composition where DP780GI-HF had a higher content of "C" and "Al".

Table 1 Chemical composition of the DP780-GI and DP780GI-HF steels

Material	Chemical composition [wt.%]						
DP780GI DP780GI-HF	C	Mn	Si	P	Al	Cr+Mo	Nb+Ti
	max. 0.18	max. 2.1	max. 0.14	max. 0.04	max. 0.7	max. 1.0	max. 0.15

Mechanical properties of the materials were determined according to STN EN ISO 6892-1 standard with testing by the Zwick / Roell Z050 device in the three different diretion, 0 °, 45 ° and 90 °. The normal anisotropy of both investigated material concepts was determined according to STN EN ISO 10113 and the strain hardening exponent "n" according to STN EN ISO 10275, on standardized samples shown in **Fig. 2**.

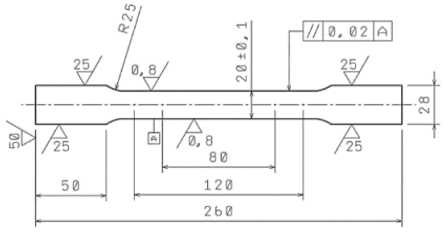

Fig. 2 Standardized sample for tensile test

The SEM methodology was used to evaluate the microstructures. Metallographic preparation was performed by grinding the samples and then polishing them with a diamond paste with grain size of 1 - 3 μm. Etching of samples was performed in 3 % Nital. Observation of the microstructure was performed using a TESCAN VEGA 3 scanning electron microscope.
To determine the FLC curves of both materials, the method of determining the limit deformations based on the so-called Nakajima stretch tests according to EN ISO 12004-2 was used, using a 100mm diameter ball drawing punch, as shown in **Fig. 3**.

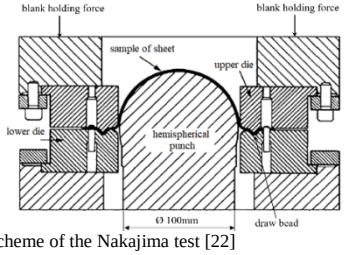

Fig. 3 Scheme of the Nakajima test [22]

Metal sheet samples of various widths, were used to construct the FLC as are given at **Fig. 4**. A shank for different sample widths was prepared by milling so that it was possible imitate all the assumed stress-strain states (uniaxial stress), surface stress (biaxial stress) and stretching (biaxial stress) that occur during real stamping. The edges of the individual samples were modified so that the microcracks after mechanical processing did not initiate premature failure of the samples. Subsequently, an irregular stochastic pattern (white background and black dots) was sprayed on the surface of the samples.
The samples thus prepared were subjected to plastic deformation on an ERICHSEN 145/60 hydraulic test machine with a maximum holding force of 250 kN. The test was performed at a constant drawing punch speed of 1 mm/s^{-1} until the sample was broken. To reduce friction between the tool and the testing samples a thin PTFE film 0.05 mm thick was used in combination with lubricating oil.

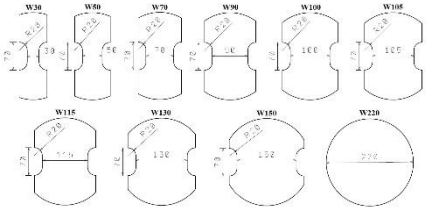

Fig. 4 Geometry of specimen according to EN ISO 12004-2

The local relative deformations occurring on the sheet surface were scanned, measured and recorded using a 3D optical system ARAMIS from GOM, **Fig. 5**.

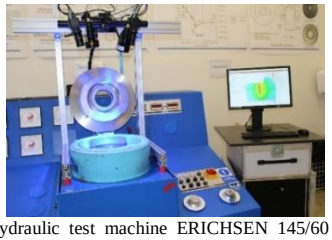

Fig. 5 Hydraulic test machine ERICHSEN 145/60 with 3D optical ARAMIS system

Based on the relative deformations, the actual deformations were determined (radial φ_1 and tangential φ_2) and subsequently the normal deformation φ_3 was calculated from the law of constant volume:

$$\varphi_1 = \ln(1+\varepsilon_1) \quad (1.)$$

$$\varphi_2 = \ln(1+\varepsilon_2) \quad (2.)$$

$$\varphi_1 + \varphi_2 + \varphi_3 = 0 \quad (3.)$$

$$\varphi_3 = -(\varphi_1 + \varphi_2) \quad (4.)$$

where ε_1, ε_2 are relative deformations.
Identification of the onset of plastic deformation of sheets at planar stress is important especially in modeling of stamping processes. Also, the onset of plastic deformation is less clear at biaxial stress than at uniaxial stress.
In order to determine the maximum size and course of shape change of the plastically deformed material, the deformation intensity φ_i was calculated from all three values of the actual deformations φ_1 φ_2 φ_3 for the selected stress states (sample widths) according to relation (5). The intensity of deformation, also called effective deformation, expresses the cumulative effect of all three deformation components on the size and course of the shape change of the stamped samples according to the formula:

$$\varphi_i = \frac{\sqrt{2}}{3} \cdot \sqrt{(\varphi_1 - \varphi_2)^2 + (\varphi_2 - \varphi_3)^2 + (\varphi_3 - \varphi_1)^2} \quad (5.)$$

To determine the proportion of phase composition for individual states of DP780GI-HF material stress, X-ray diffraction (XRD) analysis was used using a SEIFERT XRD 3003/PTS diffractometer equipped with Co-source Kα radiation (λ = 0.179026 nm). TOPAS software was used to perform Rietveld refinement of diffraction pattern / recording (measured range 45 ° – 130 ° 2 theta). Important parameters of X-ray measurement are presented in **Table 2**.

Table 2 The measurement conditions of X-ray

Generator	45 kV, 35 mA
X-ray radiation	Co- line focus
Filter	Fe
Scan step	0.02 theta
Range of measuring	45 - 130° 2theta
Input slits	3 mm, 2 mm
PSD Detector	Meteor1D

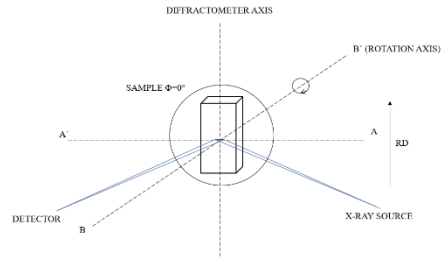

Fig. 6 X-ray measurement scheme

Samples for X-ray diffraction analysis were taken from flat sheet samples - area not affected by deformation (original / reference state) and subsequently from FLC samples after plastic deformation (local area near failure or crack). The scheme of the diffractometer together with the location of the analyzed sample is shown in **Fig. 6**. Metallographically prepared sheet samples were placed in a goniometer holder so that the 0 ° sample rolling direction was parallel to the axis of the diffractometer. During X-ray analysis, the samples rotated smoothly around the BB´ axis.

RESULTS AND DISCUSSION

SEM analysis of DP780GI grade samples shown in **Fig. 7a** pointed to a two-phase composition in which the base is ferritic matrix reinforced with martensite islets. X-ray analyses confirmed the presence of residual austenite (RA), in the volume of 2.90 wt.%.
The microstructure of two-phase steels was achieved by using to the two procedures: Top-Down using controlled cooling from the austenitic and Bottom-Up using intercritical annealing at austenitic-ferritic phase, where part of the austenite is transformed to ferrite and the remaining part of the austenite is transformed to martensite by rapid cooling. In the final microstructure of DP steels, a portion of residual austenite RA may also appear, which is transformed to martnesite by the action of external loads [2, 4, 5, 7]. A typical phase ratio is 70-90 % ferrite and 10-30 % martensite [2, 4, 6, 22, 25]. This high-strength steel is characterized by high absorption capacity and fatigue resistance, therefore these materials are used for safety parts of the car body, reinforcements and longitudinal beams [7, 11, 17, 20, 21].
In the microstructural analysis of DP780GI-HF sample (**Fig. 7b**) the presence of the bainite phase can be observed in addition to the typical ferritic-martensitic phase. The results of X-ray analysis also confirmed the presence of residual austenite, in volume of 14.99 wt.%, which is a significantly higher amount compared to the DP780GI grade.
The author [22] detected the presence of two RA fractions, namely block RA and lamellar RA in TRIP steels with higher Al content and lower Si content. From the metallographic evaluation shown in Fig. 7b it results that the DP780GI-HF steel examined is dominated by the block RA fraction.
The increased presence of RA in the microstructure of DP780GI-HF steel (compared to DP780GI steel) ensures significantly better plastic characteristics, with suitable weldability.

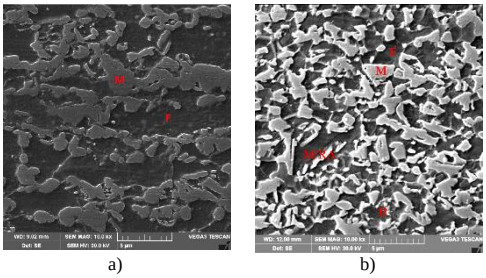

a) b)

Fig. 7 Microstructure a) DP780GI (10000x-magnification), b) DP780GI-HF (10000x-magnification)

Due to the TRIP effect that occurs during the mechanically induced transformation of RA to martensite, additional plasticity can be obtained. Compared to austenite, martensite has a higher flow stress so the transformation leads to considerable strengthening, which is beneficial for the stability of deformation [23, 24, 26].
The mechanical properties for both material concepts and their average values are given in **Table 3**.

Based on the results obtained, significant differences in elongation A_{80} and the value of n - the strain hardening exponent can be observed. While for DP780GI grade the elongation was 17.5 % and the n value was 0.116 %, for DP780GI-HF grade the ductility value was 21.6 %, and the "n" value was 0.160.

Table 3 Material properties of used steels grade, in longitudial rolling direction

Steel Grade	Thickness [mm]	YS [Mpa]	UTS [Mpa]	A_{80} [%]	r [-]	n [-]
DP780GI	1.2	484	810	17.5	0.65	0.116
DP780GI-HF	1.2	495	799	21.6	0.78	0.160

Representative stress-strain engineering curves of the two grades being compared are given in **Fig. 8a,b**. **Fig. 9a, b** show in a graphical representation the mechanical properties of both grades, in the testing directions 0 °, 45 °, 90 °. Despite the chemical similarity of the two grades compared, a difference in mechanical properties (positive increase in plasticity in DP780GI-HF grade) can be observed, which were achieved mainly by adjusting the chemical composition (C and Al contents) and heat treatment regime in the continuous annealing process and subsequent controlled cooling.

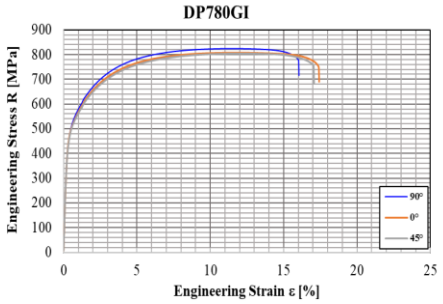

Fig. 8a Engineering Stress vs. Engineering Strain, DP780GI

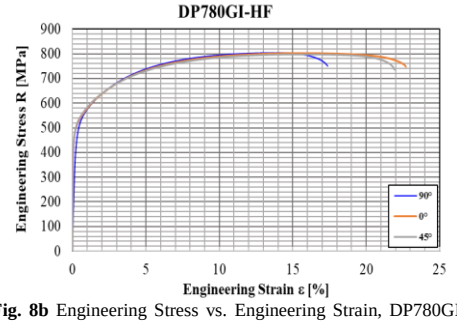

Fig. 8b Engineering Stress vs. Engineering Strain, DP780GI-HF

In order to be able to clearly determine the extent to which the deformation capabilities of the investigated DP materials are used during deep drawing or stretching, it was necessary to know unambiguously for all stress states (actual limit deformations) that occur during surface forming. The experimentally determined FLC curves were used and analyzed in relation to the evaluation of the material plasticity (sheet), i.e. by comparing their plastic properties at a specified range of stress state.
The measurement of deformations on the surface of plastically deformed samples was carried out using the method of sections from the so-called deformation history recorded by 3D optical measuring system ARAMIS. Measurement of real deformations φ_1 and φ_2 was performed several steps before the failure. After the analysis of the maximum deformations, it was necessary to determine 3 parallel sections and then determine the limit deformations for each sample width (30, 50, 70, 90, 100, 105, 115, 130, 150 and 220 mm). Each sample represents a different deformation state. Subsequently, these limit deformations were statistically evaluated for all deformation states and FLC curves were determined for both materials (**Fig. 10**), according to EN ISO 12004-2 standard.

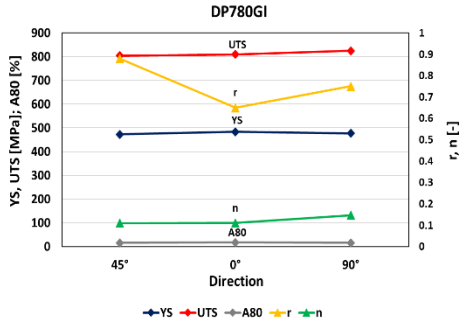

Fig. 9a Mechanical properties of DP780GI

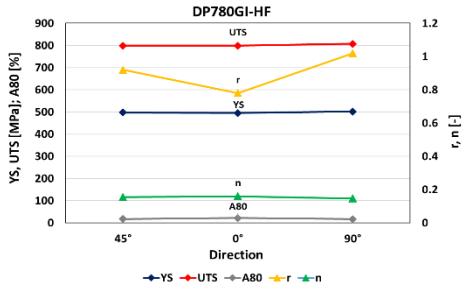

Fig. 9b Mechanical properties of DP780GI-HF

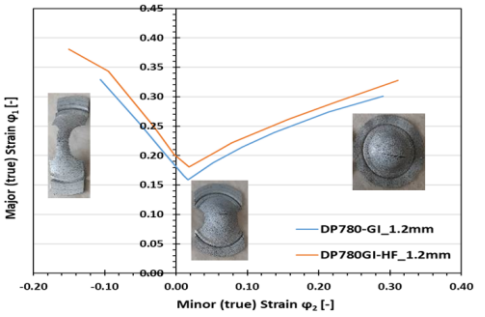

Fig. 10 Position of experimental FLC curves of both materials in the FLD diagram (limit deformation diagram)

By analyzing and comparing the plastic properties of both materials at a given stress state, the improved stampability of DP780GI-HF grade was noted. This manifested itself in the entire range of plastic deformations, i.e. by shifting the position of the FLC and thus by increasing the limit of maximum

deformations upwards into the area of permissible plastic deformations.
The FLC curve (left side of FLD) is determined for the DP780GI-HF grade by the linear regression equation:

$$\varphi_1 = - 1.2499*\varphi_2 + 0.2062 \quad (6.)$$

where the intersection $\varphi_2 = 0$ is the value 0.2062 and the regression coefficient $R^2 = 0.9809$. The right side of the FLD diagram of this grade is also determined by the linear regression equation:

$$\varphi_1 = - 0.4883*\varphi_2 + 0.1775 \quad (7.)$$

where the intersection $\varphi_2 = 0$ is the value 0.1775 and the regression coefficient $R^2 = 0.9944$.
The FLC curve (left side of FLD) is determined for the DP780-GI grade by the linear regression equation:

$$\varphi_1 = - 13904*\varphi_2 + 0.1821 \quad (8.)$$

where the intersection $\varphi_2 = 0$ is the value 0.1821 and the regression coefficient $R^2 = 0.9998$. The right side of the FLD diagram of this grade is also determined by the linear regression equation:

$$\varphi_1 = - 0.4985*\varphi_2 + 0.1593 \quad (9.)$$

where the intersection $\varphi_2 = 0$ is the value 0.1593 and the regression coefficient $R^2 = 0.99843$.

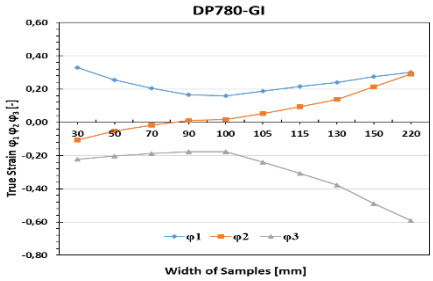

Fig. 11 Comparison of actual deformation courses for individual DP780-GI sample widths

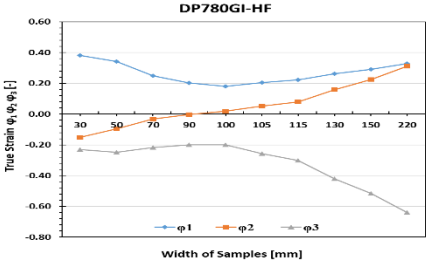

Fig. 12 Comparison of actual deformation courses for individual DP780GI-HF sample widths

These experimentally determined FLC curves of both tested materials can also be used in relation to the complex stress-strain analysis of different types of stampings and also in numerical simulations of forming processes as the most important material characteristic determining the stampability of the given material.
For the analysis of all three components of deformation φ_1, φ_2 and φ_3 at different stress states, a graphical evaluation and comparison (for both grades) of their courses was performed, see **Fig. 11** and **Fig. 12.** In terms of the location of plastic deformation for complex shape stampings, the thing of greatest importance is the normal deformation φ_3, in the direction of material thickness, which determines the place of the smallest thickness - the greatest thinning of the sheet. Due to the nature of the deformation state, the highest deformation φ_3 (plastic deformation at the expense of thickness) was manifested by an increase in the width of samples at more-axial stress (area of the right side of the FLD), while at uniaxial stress it was without thickness change.
To confirm the positive increase in plasticity of DP780GI-HF steel due to the higher RA content of 14.99 wt% detected in the microstructure (compared to DP780GI steel with detected RA content of 2.9 wt.%), and its subsequent transformation to martensite during plastic deformation, the X-ray diffraction (XRD) method was used to determine the phase composition.
Fig. 13 shows samples of DP780GI-HF grade after the stretch test, or before sampling for XRD diffraction analysis.

Fig. 13 Samples after the stretch test - determination of residual austenite in the crack area

The following phases were used to refine the measured diffraction records: Fe alfa – ferrite (grupa I m -3 m) and Fe gama – Residual Austenite (grupa F m -3 m). **Table 4** shows the identified structural phases of all tested samples.

Table 4. Phase composition of tested samples

Width of samples	Identified phase composition	
	Ferrite (229) I m -3 m [wt.%]	**Residual Austenite** (225) F m -3 m [wt.%]
1. original DP780GI	97.10wt	2.90
2. original DP780GI - HF	85.01	14.99
(30) DP780GI - HF	99.00	1.00
(50) DP780GI - HF	98.52	1.48
(70) DP780GI - HF	97.70	2.30
(90) DP780GI - HF	97.40	2.60
(100) DP780GI - HF	96.61	3.39
(105) DP780GI - HF	97.17	2.83
(115) DP780GI - HF	97.74	2.26
(130) DP780GI - HF	98.26	1.74
(150) DP780GI - HF	98.33	1.67
(220) DP780GI - HF	100.00	0.00

Fig. 14 shows diffraction recordings comparing baseline states (states before deformation - stretch test) of DP780GI and DP780GI-HF steels.
Two phases were identified in the measured diffraction patterns of the samples: ferrite and residual austenite. The percentage of

both phases was determined in the samples. All diffraction recordings were refined by the TOPAS program. From these records (**Fig. 14**), and from **Tab. 4**, we can observe a significant increase in the portion of RA in DP780GI-HF steel in the baseline state before stretching, at 14.99 wt.%, while in DP780GI steel it was only at 2.90 wt%.

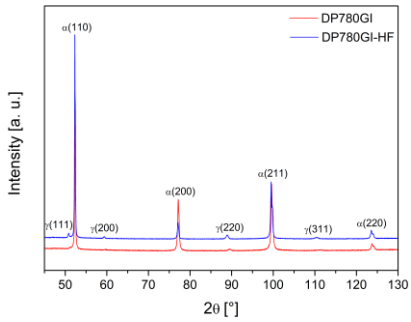

Fig. 14 Comparison of X-ray diffraction patterns for dual phase steel DP780GI and DP780GI-HF in original states

Fig. 15 shows diffraction patterns for DP780GI-HF steel comparing the state before deformation, with the individual states after plastic deformation (stretch test). The marked red area in **Fig. 16** represents the change of RA for γ (220), for individual sample widths (deformation states).

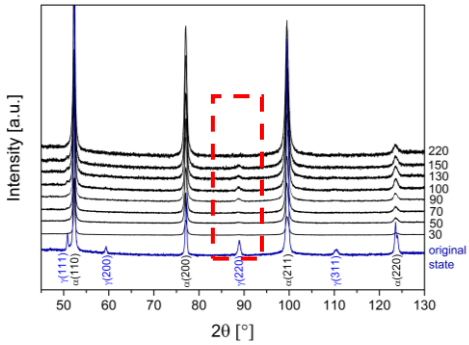

Fig. 15 X-Ray diffraction patterns for dual phase steel DP780G-HF in original state (non-deformed) and after deformation with different width of samples

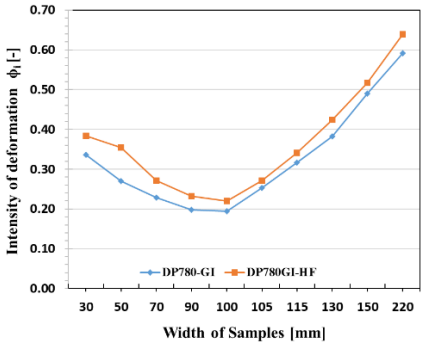

Fig. 16 Course of intensity of deformation ϕ_i for the individual sample widths of both grades

Based on the phase analysis of individual samples (grade DP780GI-HF) with different widths, it can be stated that in the area of uniaxial stress state (left side FLD - Fig. 10) the portion of residual austenite was in the range of 1.0-2.60 wt.%. Also in the area of biaxial stress - stretching (right side of FLD), the portion of residual austenite was determined in the range of 0.0-2.83 wt.%. In contrast, in the area of planar deformation (FLD_0), the highest value of residual austenite up to 3.39 wt.% was identified.

Based on **Fig. 16** it can be stated that in the areas where the largest deformations occur, the intensity of deformation also increases. Also, the deformation intensity values for all DP780GI-HF grade deformation states were situated higher compared to the conventional DP780-GI.

From the relation of RA = f (width of samples) and the calculated intensity of deformation plotted on the minor axis y ϕ_i = f (sample width) for DP780GI-HF grade (**Fig. 17**) it is clear that the effect of increased deformation intensity at biaxial loading $\phi_1 = \phi_2$ (right side of the FLD), results in a greater amount of depleted residual austenite in the material. Also due to the increased intensity of deformation at uniaxial stress $\phi_1 = -\phi_2$ (left side of FLD), there is a greater amount of depletion of residual austenite in the material. Graphical comparison and evaluation of the effect of residual austenite (RA) on the intensity of deformation ϕi for individual sample widths (stress deformation states) it can be stated that the portion of residual austenite in the material decreases due to the increase of the deformation intensity. The lowest value of the deformation intensity was recorded in the area of planar deformation (ϕ_2 = 0) - also referred to as FLD0 and thus in this deformation state the highest value of RA was determined.

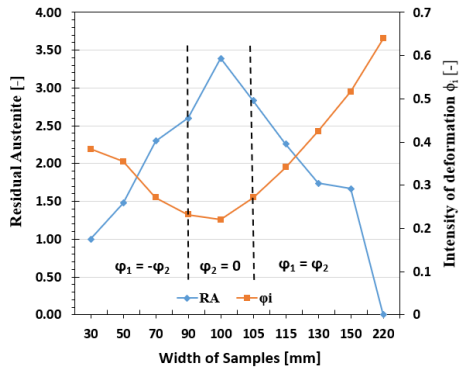

Fig. 17 Dependence of residual austenite RA on deformation intensity ϕ_i for individual widths of DP780GI-HF grade samples

CONCLUSIONS

Based on the extensive experimental research and achieved results described in this article, it is possible draw following conclusions:

- The metallographic analysis of DP780GI steel cofirmed the ferritic-martensitic microstructure, XRD diffraction analysis also confirmed the presence of the minor component RA in the volume of 2.90 wt.%. In addition to ferrite and martensite, probably minor components of bainite were detected in the microstructure of DP780GI-HF steel. XRD diffraction analysis revealed the presence of RA in this steel in the volume of 14.99 wt.%.

- For the DP780GI-HF steel, the portion of residual austenite in the range of 1.0-2.60wt.%, in the area of uniaxial stress state (left side FLD) was determined. In the area of biaxial stress - stretching (right side of FLD), the portion of residual austenite was determined in the range of 0.0-2.83wt.%. Vice-versa, in the area of planar deformation (FLD0), the highest value of residual austenite up to 3.39wt.% was identified.
- For the DP780GI-HF, the lowest value of the deformation intensity 0.22 was evaluated in the area of planar deformation ($\phi_2 = 0$). In this deformation state the highest value of RA=3.39wt.% was determined. The highest value of the deformation intensity 0.64 was evaluated in the area of biaxial stress – stretching ($\phi_1 = \phi_2$). In this deformation state the lowest value of RA=0wt.% was determined.
- Higher achieved plastic values of steel DP780GI-HF in comparison with steel DP780GI, observable especially with parameters A80 = 21.6 vs. 17.5[%] and the strain hardening exponent (n-value) = 0.16 vs. 0.116[-] are demonstrably achieved by a higher proportion of RA = 14.99 vs. 2.90wt.%, respectively.

REFERENCES

1. H. Hofmann, D. Mattissen, T. W. Schaumann: Steel Research International, 80(1), 2009, 22-28. https://doi.org/10.2374/SRI08SP113.
2. T. Kvačkaj, J. Bidulská, R. Bidulský: Materials, 14(8), 2021, 1988. https://doi.org/10.3390/ma14081988.
3. Ch. Lesch, N. Kwiaton, F. B. Klose: Steel Research International, 88(10), 2017, 1700210. https://doi.org/10.1002/srin.201700210.
4. P. Prislupcak, T. Kvackaj, J. Bidulska, P. Zahumensky, V. Homolova, P. Zimovcak: Acta Metallurgica Slovaca, 27(4), 2021, 207-209. https://doi.org/10.36547/ams.27.4.1306.
5. W. Bleck, S. Papaefthymiou, A. Frehn: Steel Research International, 75(11), 2004, 704-710. https://doi.org/10.1002/srin.200405831.
6. W. Bleck, K. Phiu-On: Material Science Forum, 500-501, 2005, 97-114. https://doi.org/10.4028/www.scientific.net/MSF.500-501.97.
7. T. Kvačkaj, J. Bidulská: Materials Science Forum, 783-786, 2014, 842-847. https://doi.org/10.4028/www.scientific.net/MSF.783-786.842.
8. A. Ramazani, Z. Ebrahimi, U. Prahl: Computational Materials Science, 87, 2014, 241-247. https://doi.org/10.1016/j.commatsci.2014.01.051.
9. O. Bouaziz, H. Zurob, M. Huang: Steel Research International, 84(10), 2013, 937-947. https://doi.org/10.1002/srin.201200288.
10. W. Bleck, X. Guo, Y. Ma: Steel Research International, 88(10), 2017, 1700218. https://doi.org/10.1002/srin.201700218.
11. L. Liu, B. He, M. Huang: Advanced Engineering Materials, 20, 2018, 1701083. https://doi.org/10.1002/adem.201701083.
12. O. Bouaziz, S. Allain, C.P. Scott, P. Cugy, D. Barbier: Current Opinion in Solid State and Material Science, 15(4), 2011, 141–168. https://doi.org/10.1016/j.cossms.2011.04.002.
13. P. Mulidran, E. Spisak, M. Tomas, J. Majernikova, J. Varga: Acta Metallurgica Slovaca, 27(3), 2021, 103-108. https://doi.org/10.36547/AMS.27.3.899.
14. T. Kvačkaj, J. Bacsó, J. Bidulská, M. Lupták, I. Pokorný, M. Kvačkaj, M. Vlado: Acta Metallurgica Slovaca, 16(4), 2010, 268-276.
15. M. Maleki, H. Mirzadeh, M. Zamani: Steel Research International, 89(4), 2018, 1700412. https://doi.org/10.1002/srin.201700412.
16. N.J. Den Uijl, L.J. Carless: Advanced Materils in Automotive Engineering, 2012, 28-56. https://doi.org/10.1533/9780857095466.28.
17. E. Evin, S. Németh, M. Tomas: Acta Metallurgica Slovaca, 21(3), 2015, 184-194. https://doi.org/10.12776/ams.v21i3.603.
18. W.F. Hosford, R.M. Caddell: Metal Forming - Mechanics and Metalurgy, 2007, 279-288. https://doi.org/10.1017/CBO9780511811111.
19. P. Mulidran, E. Spisak, M. Tomas, J. Slota, J. Majernikova: Metals, 10(9), 2020, 1119. https://doi.org/10.3390/met10091119.
20. E. Evin, M. Tomáš, J. Kmec, S. Németh, B. Katalinč, E. Wesellý: Procedia Engineering, 69, 2014, 758-767. https://doi.org/10.1016/j.proeng.2014.03.052.
21. M. Valeš, L. Chrášťanský, F. Tatíček, T. Pačák: Comparison of numerical simulation and deep drawing test of DP500 steel. In.: *27th International Conference on Metallurgy and Materials*, Tanger: Brno, Czech Republic, 2018, p. 501-506, ISBN: 978-80-87294-84-0.
22. J.R. McDermid, H.S. Zurub, Y. Bian: Metallurgical and Materials Transactions A, 42(12), 2011, 3627-3637. https://doi.org/10.1007/s11661-011-0678-z.
23. A.K. Sachdev: Acta Metallurgica, 31(12), 1983, 2037-2042. https://doi.org/10.1016/0001-6160(83)90021-4.
24. E.S. Perdahcioglu, H. J. M. Geijselaers: Materials, 15(2), 2022, 498. https://doi.org/10.3390/ma15020498.
25. D.M. Pallisco, J.R. McDermid: Material Science & Engineering, 778, 2020, 139111. https://doi.org/10.1016/j.msea.2020.139111.
26. K.M.H. Bhadhon, X. Wang, E.A. McNally, J.R. McDermid: Metals, 12(2), 2022, 356. https://doi.org/10.3390/met12020356.